Exp Fluids (2015) 56:66
DOI 10.1007/s00348-015-1934-6

RESEARCH ARTICLE

# An efficient and accurate approach to MTE-MART for time-resolved tomographic PIV

**K. P. Lynch · F. Scarano**

Received: 22 September 2014 / Revised: 18 January 2015 / Accepted: 26 February 2015


**Abstract** The motion-tracking-enhanced MART (MTE-MART; Novara et al. in Meas Sci Technol 21:035401, 2010) has demonstrated the potential to increase the accuracy of tomographic PIV by the combined use of a short sequence of non-simultaneous recordings. A clear bottleneck of the MTE-MART technique has been its computational cost. For large datasets comprising time-resolved sequences, MTE-MART becomes unaffordable and has been barely applied even for the analysis of densely seeded tomographic PIV datasets. A novel implementation is proposed for tomographic PIV image sequences, which strongly reduces the computational burden of MTE-MART, possibly below that of regular MART. The method is a sequential algorithm that produces a time-marching estimation of the object intensity field based on an enhanced guess, which is built upon the object reconstructed at the previous time instant. As the method becomes effective after a number of snapshots (typically 5–10), the sequential MTE-MART (SMTE) is most suited for time-resolved sequences. The computational cost reduction due to SMTE simply stems from the fewer MART iterations required for each time instant. Moreover, the method yields superior reconstruction quality and higher velocity field measurement precision when compared with both MART and MTE-MART. The working principle is assessed in terms of computational effort, reconstruction quality and velocity field accuracy with both synthetic time-resolved tomographic images of a turbulent boundary layer and two experimental databases documented in the literature. The first is the time-resolved data of flow past an airfoil trailing edge used in the study of Novara and Scarano (Exp Fluids 52:1027–1041, 2012); the second is a swirling jet in a water flow. In both cases, the effective elimination of ghost particles is demonstrated in number and intensity within a short temporal transient of 5–10 frames, depending on the seeding density. The increased value of the velocity space–time correlation coefficient demonstrates the increased velocity field accuracy of SMTE compared with MART.

K. P. Lynch (✉) · F. Scarano
Aerospace Engineering Department, Delft University of Technology, 2629 HS Delft, The Netherlands
e-mail: k.p.lynch@tudelft.nl

## 1 Introduction

Time-resolved tomographic PIV is a specific measurement regime of the tomographic PIV technique (Elsinga et al. 2006) characterized by a high degree of spatial and temporal coherence between subsequent measurements. In practice, this is realized using high-speed camera and laser systems to acquire image sequences typically composed by hundreds or thousands of recordings. When the system operates in sequential mode, the images are recorded at a time separation that is small enough to enable their cross-correlation. As a result, the spatial and temporal development of a flow is vividly captured. The breadth of information contained in these sequences has led to its application to investigate unsteady flow phenomena (see, e.g., the panel of applications in the review of Scarano 2013). Among the most prominent applications of time-resolved tomographic PIV are the unsteady pressure evaluation (van Oudheusden 2013), aeroacoustic estimation (Violato and Scarano 2013; Probsting et al. 2013) and the study of fundamental mechanisms in turbulent shear flows (Elsinga and Marusic 2010; Schroeder et al. 2011).

A constraining factor in all tomographic PIV experiments is the measurement error introduced by reconstruction. The error has multiple sources: imaging artifacts

Published online: 13 March 2015

(e.g., out-of-focus blur, Schanz et al. 2013a), calibration inaccuracies (Wieneke 2008), background reflections and camera noise; however, the predominant source is due to ghost particles (Elsinga et al. 2006). At a low-to-moderate level of particle image density (e.g., for a system of four cameras and particles per pixel, ppp < 0.05), the peak intensity of ghost particles is significantly lower than that of actual particles and their effect on cross-correlation can be neglected. However, experiments requiring high spatial resolution involve a greater particle concentration, leading to increased particle image density (i.e., ppp > 0.1). In this regime, ghost and actual particles share similar peak intensity, with significant detrimental effect on the cross-correlation (Elsinga et al. 2011).

This limitation has motivated multiple efforts to reduce the number and intensity of ghost particles in the reconstruction. The spatial filtering improved reconstruction (SFIT) approach by Discetti et al. (2013) uses a tailored filtering of the reconstructed volume between reconstruction iterations to regularize reconstructed particle shapes and partly filter out ghost particles. The simulacrum matching-based reconstruction enhancement (SMRE) technique proposed by de Silva et al. (2013) removes ghost particles a posteriori of the reconstruction process based on some hypotheses on the shape of the particles. Another a posteriori approach by Elsinga and Tokgoz (2014) is based on particle tracking velocimetry (PTV). With a long sequence of time-resolved images, ghost particles could be unambiguously identified and removed.

A substantial reduction in ghost particles has been achieved using methods that exploit the coherence of particles over two or more frames within the reconstruction. The first method in this category is the motion-tracking-enhanced MART (MTE-MART; Novara et al. 2010). The working principle is the combined use of recordings taken non-simultaneously to produce an enhanced first guess for the tomographic reconstruction algorithm. The method features an iterative procedure of reconstruction and cross-correlation whereby the velocity field is used to deform the reconstructed object and obtain an enhanced initial guess for the reconstruction at a different time instant. Its application to turbulent shear flows (Novara and Scarano 2012) showed that a seeding density up to 0.2 ppp could be afforded by a four-camera system. It was concluded that MTE-MART makes a significant improvement with respect to regular MART when a kernel of 3–5 exposures is considered. However, in the latter conditions, the computational effort becomes more than one order of magnitude greater than the standard method, based on MART reconstruction followed by cross-correlation analysis. This is due to the iterative approach applied to the whole time kernel to obtain the reconstruction at a given time instant. Efficient reconstruction procedures such as MLOS-SMART have been proven compatible with the MTE principle and alleviate the computational burden (Atkinson et al. 2010). However, for time-resolved tomographic PIV, where thousands of images are involved, the additional computational cost of all MTE methods has so far precluded its widespread use, possibly resulting in a stagnation of developments on this topic.

The second method in this category is the recently introduced ‘shake-the-box’ (STB) method of Schanz et al. (2013b), which combines 3-D PTV with the iterative particle reconstruction (IPR) method of Wieneke (2013). Particles are tracked in 3-D space over multiple frames providing a Lagrangian description of the fluid motion and clear discrimination criteria for the elimination of ghost particles from reconstructions. Furthermore, the method is computationally efficient in comparison with the voxel-based reconstruction procedures. The STB method has been first applied to water flows using a tomographic system composed of six high-speed cameras. A recent numerical evaluation of the method (Schanz et al. 2014) has shown the ability of STB to strongly remove ghost particle intensity for time-resolved sequences.

The present article recognizes the principle of motion tracking in image sequences for enhancing the tomographic reconstruction and proposes a novel implementation of MTE-MART that exploits the potential of this concept in terms of both computational efficiency and attainable accuracy. The working principle is first elucidated, followed by a detailed assessment based upon a synthetic time-resolved tomographic PIV experiment of a turbulent boundary layer with data produced from a direct numerical simulation (Probsting et al. 2013). The experimental verification makes use of the time-resolved image sequence proposed by Novara et al. (2012) regarding the turbulent wake behind the trailing edge of an airfoil. A second experiment of a swirling jet illustrates the potential of SMTE for accurate reconstruction using a three-camera tomographic system.

## 2 SMTE working principle

The primary concept of MTE-MART (Novara et al. 2010) is that subsequent exposures contain essentially the same particle field. Such information can be used in the reconstruction of a single snapshot. Because the particles appear with slightly different (relative) position along the exposures, the reconstruction can be improved by reducing the ambiguity of the MART solutions if all these views can be used to generate an a priori condition for the first guess of the MART calculation. However, for the improved reconstruction of a single snapshot, MTE makes use of a finite temporal kernel, where knowledge of the reconstructed intensity field and the velocity field at all time instants is

required. This is achieved with an iterative procedure. For time-resolved measurements, this operation can be regarded as a *time-sliding-kernel* approach for MTE evaluation. In the first iteration, the initial guess of voxel intensity for the reconstruction is set as uniform (typically unit) value. Following the discussion and the nomenclature introduced by Novara and Scarano (2012), the number of enhancement iterations $N_E$ is the primary driver of the computational cost, with typical increases of 3–10 times for analysis of an image pair ($N_O = 2$). Extending the size of the temporal kernel (effectively, the number of objects $N_O$) to three or five does yield an improved accuracy, but the computational cost increases even more rapidly. An additional bottleneck preventing the use of large kernels is the less accurate prediction of particles motion, possibly affected by truncation errors.

The main variation introduced in the present work to the MTE method is changing the *time-sliding-kernel* approach into a *time-marching* algorithm. The latter can be applied to image sequences as typically acquired in time-resolved tomographic PIV experiments. Once the velocity field associated to the first two snapshots is estimated, an enhanced initial guess for the reconstruction of the third snapshot $E_{G,3}$ can be obtained by propagating the previous reconstruction $E_2$ forward in time via the velocity field. For a generic frame number $n$, the relation reads as:

$$E^G_{n+1} = E_n(R - V'_{n+1}\Delta t) \tag{1}$$

where the vector $\boldsymbol{R} = (X, Y, Z)$ indicates object space coordinates. The propagation is identical to that followed for the image deformation methods (Huang et al. 1993; Scarano 2002) and is applied as three-dimensional (volume) deformation in this case. The sequential approach justifies the term sequential motion-tracking-enhanced MART (SMTE-MART). A schematic description of the procedure is given by the following steps and graphically illustrated with the flow chart of Fig. 1. It is assumed that the sequence starts with frame number $n = 1$:

1. Object reconstruction
   (a) If $n = 1$: reconstruct pair $E_1$ and $E_2$
   (b) If $n > 1$: reconstruct $E_{n+1}$, using initial guess $E^G_{n+1}$
2. Velocity field calculation
   (a) Cross-correlation of the pair $E_n \otimes E_{n+1}$ yields velocity $\boldsymbol{V}_n$
3. Enhanced guess estimation for the subsequent snapshot
   (a) Estimate velocity $\boldsymbol{V'}_{n+1}$ (see Eq. 2)
   (b) Build enhanced guess $E^G_{n+2}$ by deforming $E_{n+1}$ by $\boldsymbol{V'}_{n+1}$ (see Eq. 1)

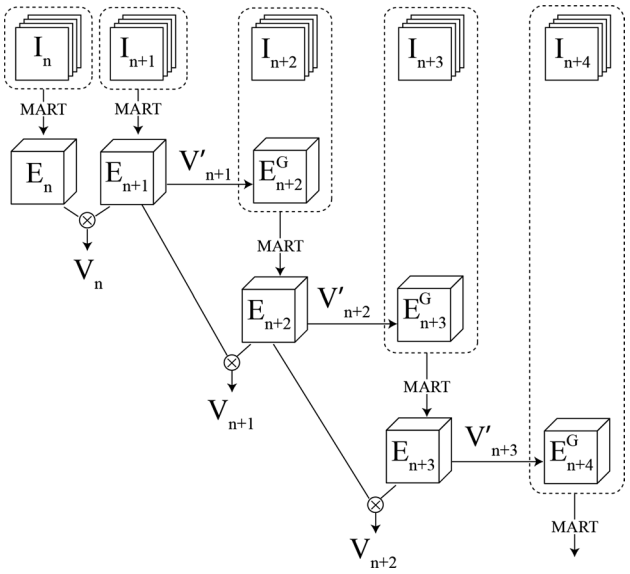


**Fig. 1** Schematic flow chart of SMTE-MART. $I_n$ indicates the set of camera images at frame $n$. *Dashed boxes* include the images and the first guess intensity field used for MART

4. Time marching
   (a) Increment $n$ and return to step (1b)

The velocity at the upcoming frame $\mathbf{V}_{n+1}$ is estimated as $\mathbf{V}'_{n+1}$ making use of a time forward approximation in the assumption of advection. This approach is valid when the time separation between frames $\Delta t$ is small relative to the flow time scales, which generally applies for time-resolved PIV sequences.

$$\boldsymbol{V}'_{n+1}(\boldsymbol{R}) \approx \boldsymbol{V}_n(\boldsymbol{R} - \boldsymbol{V}_n\Delta t) \tag{2}$$

The advection assumption was shown to yield a good approximation of the velocity temporal evolution when the two components of the material acceleration $\mathrm{d}\boldsymbol{V}/\mathrm{d}t$ and $\boldsymbol{V} \cdot \nabla \boldsymbol{V}$ are equal and opposite, yielding $\mathrm{D}\boldsymbol{V}/\mathrm{D}t \approx 0$. Under this condition, known as frozen turbulence, which occurs in turbulent flows with moderate levels of shear, the above equation was proven accurate for the prediction of the velocity in between measured time instants (time super-sampling, Scarano and Moore 2012). A more generally valid time-prediction methods (e.g., vortex-in-cell, Schneiders et al. 2014) may be considered for more complex flows (e.g., the separated region of wakes and free shear layers in jets) and when the time separation between frames is enlarged.

Two practical notes on the numerical implementation of the method should be mentioned. First, extrapolation of the object intensity in the generation of the enhanced guess should be given a nonzero value to allow the buildup by multiplicative update of the intensity along inflow

boundaries of the reconstructed domain. A practical choice proposed herein is that voxels at the volume boundary are set to a value corresponding to the mean intensity of the reconstructed volume. Second, the two snapshots at the beginning of the sequence $E_1$ and $E_2$ shall be reconstructed with the standard MART algorithm with the typical number of iterations ($N_M = 5$). This enables a faster convergence of the results along the sequence. The number of MART iterations for the following snapshots can be reduced to three or even less, as discussed in the remainder of the article.

A number of advantages are expected when the MTE principle is applied in time-marching mode along the sequence. First, the accuracy of the enhanced guess will improve throughout the sequence and increase its sparsity as the space where no particles are present is progressively determined. This condition enables to reduce the number of MART iterations needed for the convergence of a snapshot reconstruction. Second, as the effective number of exposures $N_O$ increases along the sequence, the effect of virtually multiplying the number of viewing cameras is exploited, eventually surpassing that typically achieved by MTE-MART.

The performance of the SMTE-MART algorithm follows that of MTE-MART in terms of ghost intensity suppression and enhancement of actual particles reconstruction. Also the increase in correlation signal-to-noise ratio, as discussed in Novara et al. (2010) and Novara and Scarano (2012), is retrieved back in the current study.

A topic of particular concern for time-marching algorithms is stability: For MTE-MART, it was demonstrated that the worst-case performance (e.g., due to an erroneous velocity vector field) corresponds to the standard MART solution due to the multiplicative nature of the MART update, which prevents an incorrect enhanced guess from degrading the final solution (Novara et al. 2010). The same principle applies to SMTE-MART, which therefore in the worst-case scenario corresponds to standard MART with an equal number of reconstruction iterations.

As a final note, the general nature of the sequential algorithm makes it suited to other iterative reconstruction algorithms such as MLOS-SMART (Atkinson and Soria 2009) or BIMART (Thomas et al. 2014), where further improvements may be obtained in terms of computational efficiency. Since the MART algorithm is the most widely referred to in the literature, the present study uses it for reconstruction.

## 3 Assessment from simulated turbulent boundary layer

### 3.1 Test case and data processing

The performance of SMTE-MART is first investigated in absence of calibration errors and imaging noise. Synthetic tomographic PIV images of a turbulent boundary layer over a flat plate are generated following a direct numerical simulation (DNS) from Bernardini and Pirozzoli (2011). Details of the simulation and data discretization are given in the work of Probsting et al. (2013) who verified the suitability of tomographic PIV for determining the spectral coherence of surface pressure fluctuations.

The simulated measurement domain encompasses $21.6 \times 10.8 \times 10.8$ mm$^3$ along streamwise (X), spanwise (Y) and wall-normal (Z) directions, respectively. The thickness of the turbulent boundary layer is $\delta_{99} = 12$ mm, and the associated Reynolds number is $Re_\delta \approx 8185$. The particle concentration is set to 25 part/mm$^3$, yielding a particle image density of 0.2 ppp. Particles are randomly distributed in space, and their motion is calculated from the DNS velocity fields using a fourth-order Runge–Kutta ODE solver. A thin buffer region on all boundaries is used to allow particles entering and leaving the simulated measurement domain.

The particle blobs are generated using 3-D Gaussian integration onto a voxel grid (adapted from Lecordier and Westerweel 2004). Camera images are obtained by projecting the 3-D particle positions onto 2-D sensors via a pinhole camera model (Tsai 1987) and performing 2-D Gaussian integration onto a pixel grid. The size of the projection images is $1050 \times 600$ px, with a particle image diameter of approximately 2.5 px. The simulation employs four cameras with viewing directions of 30° from the normal to the wall along both directions (cross-configuration), corresponding to a system aperture of 60° along horizontal and vertical direction, a commonly adopted and favorable configuration for tomographic imaging and reconstruction (Scarano 2013).

The tomographic reconstruction with MART follows the numerical recipe given by Elsinga et al. (2006). The number of MART iterations $N_M$ is varied in the analysis; a Gaussian smoothing of the object is applied between successive MART iterations on a kernel of $3 \times 3 \times 3$ voxels. The reconstructed volume size is $964 \times 532 \times 532$ voxels with a non-illuminated buffer of 50 voxels on each boundary that prevents edge effects in the reconstruction and allows calculating the reconstruction signal-to-noise ratio. The chosen discretization is based upon a voxel/pixel ratio of 1.0, resulting in a resolution of 40 vox/mm.

The reconstructed objects are interrogated using an in-house code based on 3-D spatial cross-correlation (Fluere) with interrogation volumes of size $28 \times 28 \times 28$ voxels and 75 % overlap factor. The average number of particles inside each interrogation volume is approximately $N_I = 8$. The cross-correlation algorithm is based on iterative volume deformation, using symmetric block direct correlation (Discetti and Astarita 2012) and Gaussian window weighting. Spurious vectors are detected by universal outlier

detection (Westerweel and Scarano 2005) and replaced with a distance-weighted neighborhood average. No spatial filtering/smoothing is applied to the final vector field. A time-marching predictor of the cross-correlation is used to bypass the need for multi-grid evaluation and accelerate the processing, as used by, e.g., Scarano and Poelma (2009).

### 3.2 Reconstruction quality

Several metrics are invoked to evaluate the accuracy of the reconstructed objects. First, the reconstructed laser sheet intensity distribution is visualized along a plane that includes the depth direction. Regions of the reconstruction within the laser sheet contain both real and ghost particles, while regions outside the laser sheet contain only ghost particles (a top-hat laser beam model was applied for the illumination). A well-accepted verification criterion for the tomographic reconstruction is the ability to clearly identify the laser sheet within the reconstructed volume (Scarano 2013). A central principle of the MTE-MART technique is the reduction in ghost particles intensity and the increase in real particles intensity (Novara et al. 2010). In Fig. 2 (right), the diagrams indicate a ratio of intensity of approximately 2.5:1 for the MART reconstruction with 5 iterations and 3.3:1 when the number of iterations is increased to 20. MTE-MART returns an intensity distribution comparable to the latter case. The application of SMTE-MART leads in practice to the elimination of ghost particle intensity. Interestingly, the same result seems to be obtained, irrespective of the number of MART iterations adopted for each snapshot.

The reconstruction signal-to-noise ratio, $SNR_R$ is defined as the ratio of mean intensity inside the and outside the illuminated region. A minimum value of 2 is considered a criterion for an acceptable reconstruction (Scarano 2013). Clearly, greater values of $SNR_R$ correspond to a reduced contribution from ghost particles. The $SNR_R$ is shown in Fig. 3. MART reconstructions with 5 or 20 iterations return values of 2.0 and 3.3, respectively. The increase in SNR with additional MART iterations is a behavior typically encountered using synthetic data where image noise is not considered. In experimental data instead (see Sect. 4), the improvement of reconstruction quality Q after 5 MART iterations becomes less pronounced. SMTE-MART begins with a reconstruction SNR equal to the MART case and increases rapidly (one order of magnitude after 5 frames) reaching a converged value (independent of further time advancement) of approximately 100 after approximately 15 frames. This result also seems to be independent of $N_M$, although the rate of convergence increases slightly with $N_M$. Remarkably, for all considered values of $N_M$, the $SNR_R$ obtained after convergence is significantly higher than MART $N_M = 20$. This indicates that the reconstruction accuracy of SMTE-MART is not only related to the larger number of MART iterations (considered along the sequence), but mainly due to the fundamental principle of MTE, whereby the particles with coherent motion are retained along several frames against the incoherent ghost particles.

A second evaluation criterion is the reconstruction quality factor Q as originally proposed by Elsinga et al. (2006), defined as the normalized cross-correlation coefficient between the reconstructed and exact object. Compared with the $SNR_R$, which is predominantly an estimate of ghost formation, $Q$ also yields a measure of the spatial accuracy in the reconstruction of actual particles.

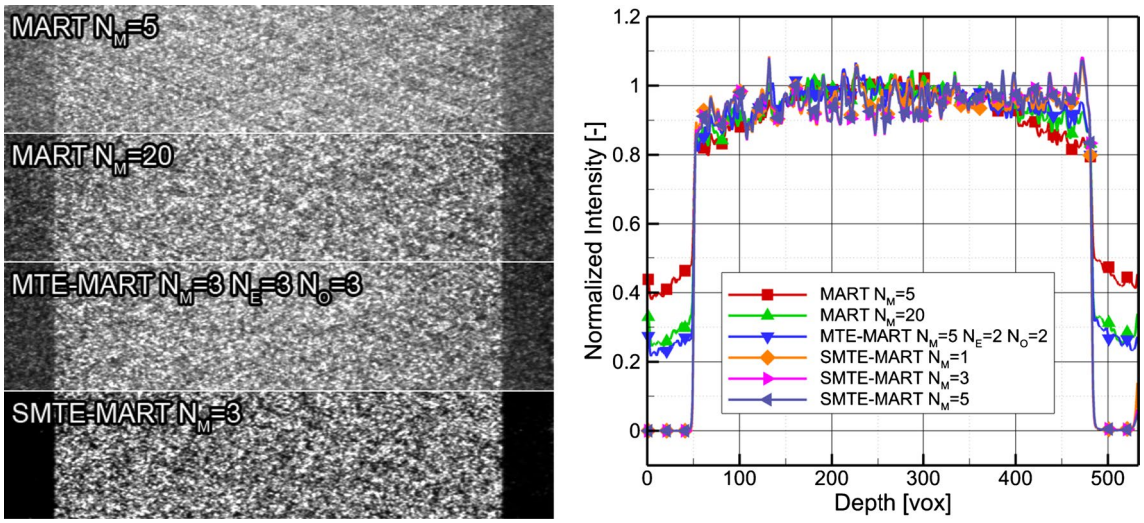


**Fig. 2** Reconstructed light intensity distributions for frame $n = 20$. *Left* Y–Z section of the volume with values averaged along the streamwise direction. *Right* reconstructed object intensity profiles along Z (depth)

For example any small positional inaccuracy due to inaccurate correction by SMTE-MART of the incoming enhanced guess would result in considerable decrease in $Q$. The results shown in Fig. 3 indicate that the above circumstance is not encountered, at least for the present case. The comparison yields $Q = 0.87$ (at all values of $N_M$) for SMTE, whereas the highest value obtained with MART at $N_M = 20$ is $Q = 0.67$, MTE-MART returns a value slightly exceeding 0.7.

The number of frames required for SMTE to reach convergence may raise issues on its application to short sequences (e.g., high-speed burst systems). However, as for any sequential algorithm, SMTE can also be applied backward in time after marching along the sequence in the forward direction. The resulting 'forward–backward' SMTE will become more computationally expensive, but still yield a benefit compared with standard MART or MTE in short sequences (typically 2–8 frames). For brevity, this mode of operation is not discussed further.

The analysis of ghost particles reduction is performed by direct inspection of occurrence and peak intensity of ghost particles within the volume. Reducing the presence of ghost particles is reported to yield an improved cross-correlation analysis as their presence potentially corrupts the cross-correlation map in proximity of the peak, resulting in a bias toward lower values of the velocity gradient (Elsinga et al. 2010).

The particle detection scheme required for this analysis assumes a 3-D Gaussian blob for the real particles. Any particle found within one voxel distance from the position of a real particle is considered a valid match. All other peaks are associated to ghost particles. A histogram of the real and ghost particle intensities for MART and SMTE is given in Fig. 4 for frame $n = 20$. The vertical axis is truncated to clearly illustrate the distribution of real particles. The MART reconstruction yields an intensity of real particles that largely overlaps with that of the ghost particles. In contrast, SMTE establishes a clear range separation between

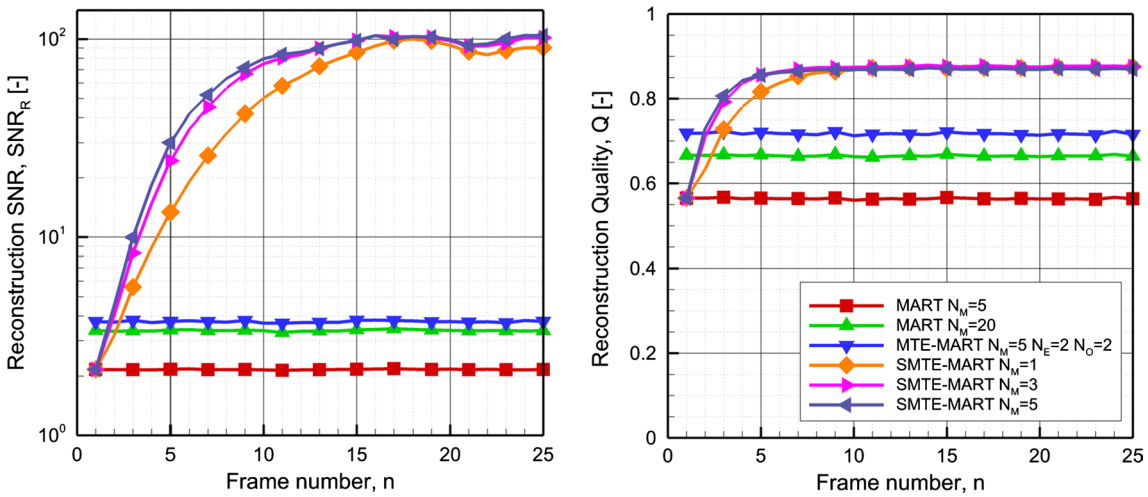


**Fig. 3** *Left* reconstruction signal-to-noise ratio $SNR_R$. *Right* reconstruction quality factor Q

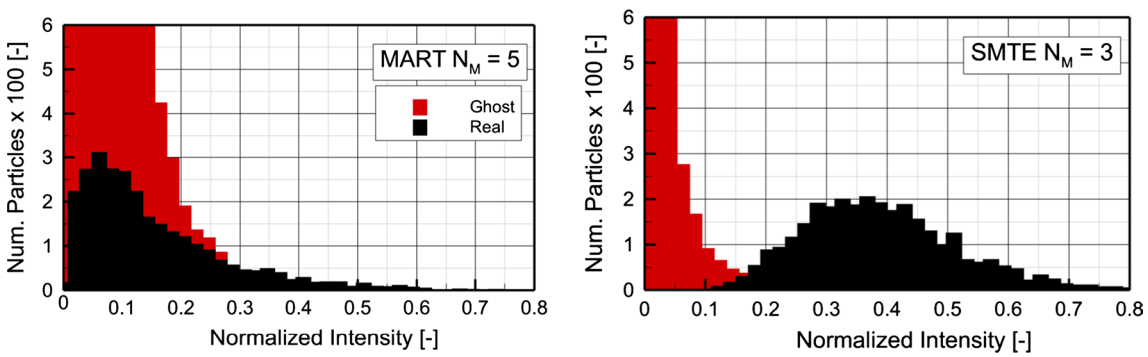


**Fig. 4** Histogram of peak intensities for MART (*left*) and SMTE (*right*). Ghost particles in *red*, real particles in *black*. Vertical axis truncated to ease visualizing the intensity distribution of real particles

peak intensity of real and ghost particles. This behavior is consistent with previous reports on MTE-MART (Novara et al. 2010).

A similar behavior is noted in the number of ghost/real particles. The ratio of generated ghost particles to real ones is approximately 25 for MART and drops to 5 for SMTE. In both cases, the number of real particles generated is nearly equal to the actual simulated particles.

### 3.3 Velocity field analysis

The velocity field accuracy is first assessed qualitatively by visual inspection of its spatial coherence in comparison with the velocity field obtained by cross-correlation analysis of the exact particle field. Furthermore, the quantitative analysis is based on the absolute error level. A visual comparison of the velocity field at frame number $n = 20$ is shown in Fig. 5. The reference case is chosen as the cross-correlation of the exact intensity field in order to account only for the errors due to the reconstruction and not those associated with the finite spatial resolution. The objects reconstructed with MART ($N_M = 5$) and SMTE-MART ($N_M = 3$) are considered. Contours of the streamwise velocity along a plane parallel to the wall and isosurfaces of positive values of the Q-criterion for visualization of vortical structures are represented. The reference velocity field features regions of high and low velocity. Around the latter, vortical structures are more often detected, elongated along the streamwise direction or under form of arcs and canes. A hairpin like structure is visualized in the top-right region of the selected field, atop an elongated low-speed region. This is consistent with the observed pattern of coherent structures in turbulent boundary layers at the current Reynolds number (Adrian 2007).

An inspection of the result obtained with the MART reconstruction yields isosurfaces with no evidence of the characteristic vortical structures. Moreover, the streamwise velocity

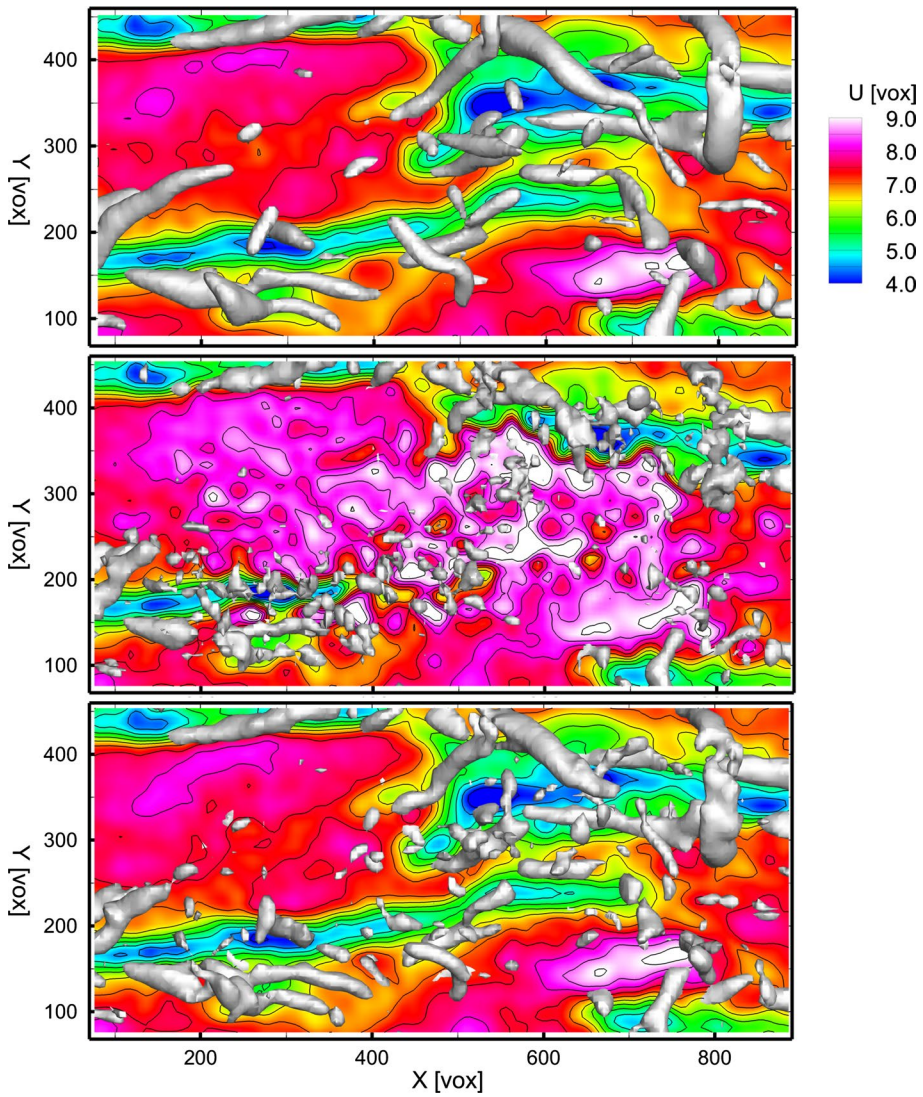


**Fig. 5** Velocity fields of frame $n = 20$. The $z$-coordinate (wall-normal) is oriented normal to the page. Isosurfaces of positive Q-criterion, contours of streamwise velocity. *Top* reference velocity field from correlation of exact objects; *center* MART $N_M = 5$; *bottom* SMTE-MART $N_M = 3$

contours, which in the reference field reveal elongated alternating streaks of high- and low-speed fluid near the wall, are less distinct with the MART reconstruction and appear generally biased toward higher velocity values. The latter is ascribed to high velocity outlier vectors due to ghost particles generated by particles in the outer layer and forming closer to the wall. The tracer particles traveling at approximately freestream velocity form the largest number of ghost particles along the entire depth of the measurement domain. Thus, the correlation near the wall with MART is heavily biased by a large number of fast-moving ghost particles, which dominate the signal against a smaller number of slowly moving actual particles subject to strongly sheared motion.

Many of the features observed in the reference velocity field can be retrieved in the analysis conducted with the objects reconstructed with SMTE. Although a higher noise level is observed, the scenario is considerably more favorable within the SMTE results, with the alternating streaks clearly identified in agreement with the reference field.

The measurement accuracy is assessed quantitatively by evaluation of the total error, determined by the RMS of the difference between the measured and actual velocity field. In Eq. 3, $i$ is the grid node index and $N$ the total number of vectors in the measurement domain.

$$\varepsilon_{\Delta x} = \sqrt{\frac{1}{N}\sum_{i=0}^{N}(\Delta x - \Delta x_{actual})^2} \tag{3}$$

The total error, varying along the sequence of frames, is reported in Fig. 6. In this case, the reference velocity field is given by the DNS data. The data series showing the smallest error (approximately 0.1 voxels) is that obtained cross-correlating the exact particle field. The level of the error associated to the analysis with 5 MART iterations is above 0.6 voxels, which compares well with a recent study of tomographic PIV measurement uncertainty from the authors (Lynch and Scarano 2014). Increasing the number of iterations to 20, the minimum error level achievable using MART is approximately 0.4 voxels. Based on the freestream displacement of 12 voxels, the corresponding dynamic velocity range (DVR; Adrian 1997) of this simulated measurement reduces to only 30 levels. The SMTE result converges to a total error between 0.15 and 0.2 voxels, depending on the number of MART iterations. The close approximation to the result obtained cross-correlating the reference objects indicates that SMTE has reduced the occurrence of ghost particles to a level that is negligible.

### 3.4 Computational time

The computational effort required to realize MTE-MART was already reported as being much greater than standard MART processing (Novara et al. 2010). Given that MART calculations are already computationally demanding, the application of MTE-MART has become impractical for large image sequences. In contrast, the SMTE-MART procedure does not require additional iterations and achieves a superior result to both standalone MART and MTE even when fewer MART iterations are used. The only additional computational step over MART is the generation of the enhanced guess. The computational cost is summarized in Fig. 7, where the approximate wall-clock time required for each of the processing tasks is shown. The computation time is broken into segments for reconstruction, correlation and (in the case of MTE and SMTE) enhanced guess generation. The

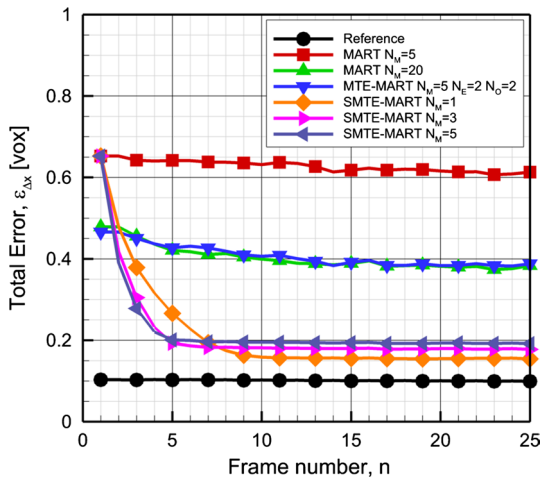


**Fig. 6** Total RMS error. *Reference curve* indicates correlation performed on reference objects (no reconstruction errors)

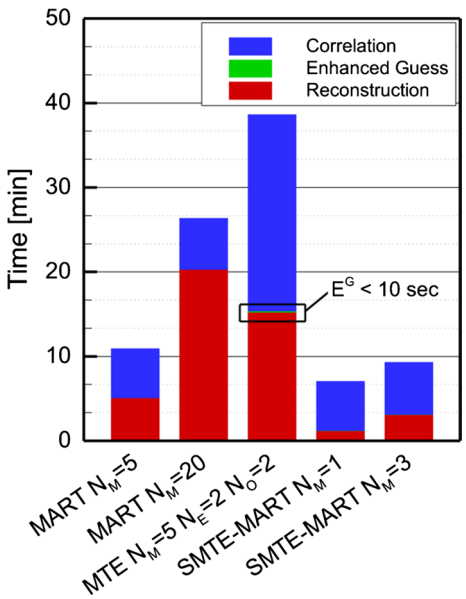


**Fig. 7** Approximate wall-clock time for a single snapshot reconstruction using MART, MTE and SMTE processing

result is averaged over the 25 frames considered, not including the initial reconstructions performed using 5 MART iterations. The wall-clock time is approximated by dividing the CPU time by the number of CPU cores (presently 48).

Both the SMTE $N_M = 1$ and $N_M = 3$ results have a computation time shorter than even the standalone MART, at under 10 min per frame. Furthermore, the computational load of cross-correlation exceeds that of the reconstruction. In contrast, the case of MART $N_M = 20$ takes four times as long to reconstruct as the MART $N_M = 5$ case, but with an identical time spent in cross-correlation. Finally, the MTE is longer in both reconstruction and cross-correlation due to the iterative procedure. In total, the SMTE approach results in a method over four times faster than MTE and marginally less time consuming when compared to MART.

## 4 Experimental assessment of a turbulent trailing edge

### 4.1 Test conditions and measurement apparatus

The present analysis follows closely that performed by Novara and Scarano (2012). Data are gathered from a time-resolved tomographic PIV experiment on turbulent flow past the trailing edge of an airfoil. Details of the experiment are provided in Ghaemi and Scarano (2011).

The airfoil model is a NACA-0012 of 40 cm chord placed at zero angle of attack. The freestream velocity is 14 m/s, yielding a chord Reynolds number of 370,000. The boundary layer thickness $\delta_{99}$ at the trailing edge is 9.5 mm. At this location a measurement volume of 40 × 24 × 8 mm is realized. The experimental apparatus consists of a Quantronix *Darwin-Duo* Nd:YLF laser (2 × 25 mJ/pulse at 1 kHz) and four high-speed Photron *Fastcam SA1* CMOS cameras (1024 × 1024 pixels at 5400 fps). The illumination is increased by the multi-pass technique, reflecting the beam multiple times throughout the volume (Ghaemi and Scarano 2010). Seeding is provided by a stage smoke generator producing particles with 1 μm nominal diameter.

The cameras are fitted with 105 mm focal length Nikon objectives operating at $f/\# = 22$ and arranged in a linear configuration (see Fig. 8). The particle image diameter $d_\tau^*$ is 1.5 px as determined via autocorrelation analysis. Both the laser and camera systems are operated in single-frame continuous mode to record a time-resolved image sequence at a frequency of 12 kHz. Synchronization and image acquisition are controlled from a PC with LaVision DaVis 7.4 software and a high-speed controller.

Two experiments are conducted at a particle image density of 0.05 and 0.2 ppp. These correspond to particle concentrations of 3 and 12 particles/mm$^3$, respectively. Details on the particle density estimation can be found in Novara and Scarano (2012). Image preprocessing consists of two steps: First, the historical minimum is calculated at each pixel for each camera. Then, the images are subtracted by the corresponding minimum. The images are further divided by the time-average value at each pixel to normalize the intensity within each camera image and among cameras. No spatial filtering (smoothing) is applied. Example preprocessed images are given in Fig. 8.

The case ppp = 0.05 is used to refine the camera mapping functions via the volume self-calibration technique (Wieneke 2008). Residual calibration errors are below 0.1 pixels. The reconstructed volume is discretized by 900 × 550 × 250 voxels with a pixel-to-voxel ratio of 1.0. The cross-correlation analysis is identical to the synthetic

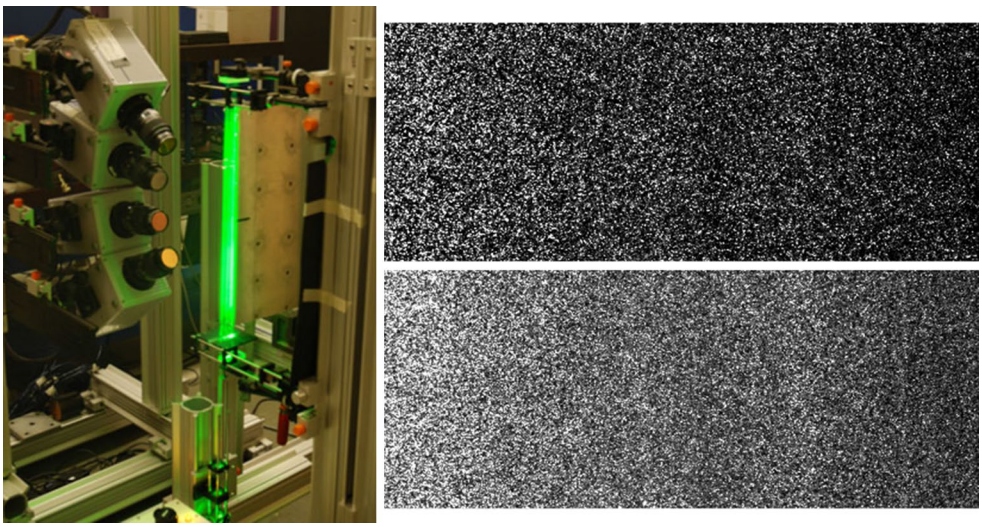

**Fig. 8** *Left* tomographic PIV setup (reproduced from Ghaemi and Scarano 2011). *Right* individual particle images after preprocessing (cropped to 500 × 200 pixels) at ppp = 0.05 (*top*) and 0.2 (*bottom*)

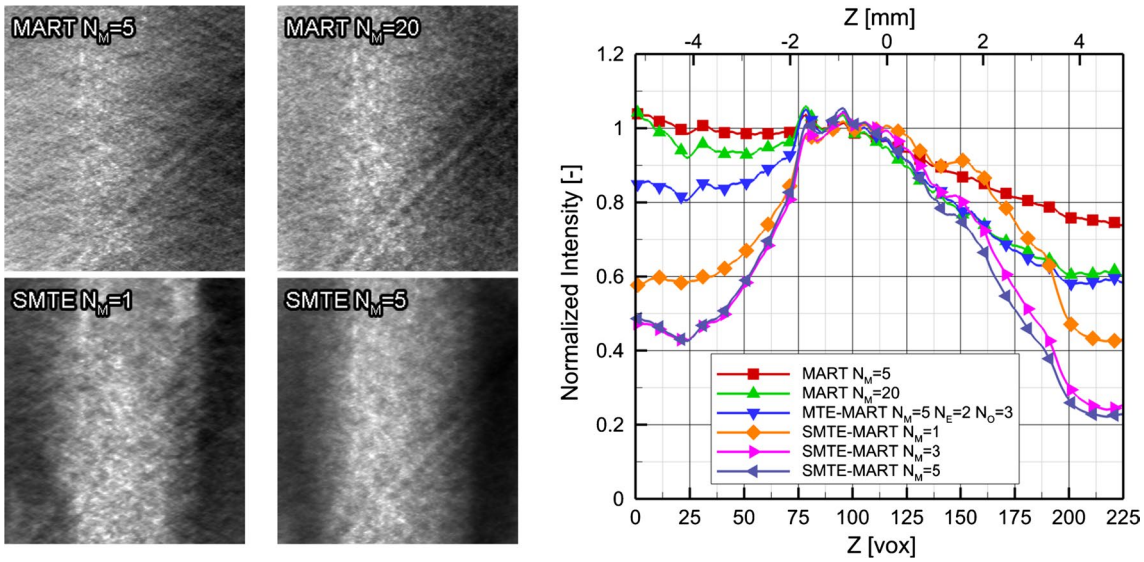


**Fig. 9** Reconstructed light intensity distributions for frame $n = 30$ to 35. *Left* reconstructed intensity distributions, summed along streamwise direction. *Right* reconstructed intensity profiles, summed along streamwise and transverse directions

case, but using interrogation volumes of 24 × 24 × 24 voxels (1.2 × 1.2 × 1.2 mm$^3$) at 75 % overlap. This corresponds to $N_I = 15$ particles within an interrogation region for ppp = 0.2.

### 4.2 Reconstruction quality

The laser sheet intensity distribution for the reconstructed volume of frame 35 in the sequence is given in Fig. 9. The MART ($N_M = 5$) reconstruction has an intensity distribution that does not exhibit any region with higher intensity. Therefore, also the edges of the illuminated region are not visible. Increasing iterations ($N_M = 20$) and using the MTE-MART deliver a small region of local maximum barely distinguishable above the background level. With the introduction of SMTE-MART the boundaries of the illuminated volume become better defined. Note that the SMTE-MART $N_M = 1$ (a single MART update), although better than regular MART and MTE-MART, is less defined than the cases with additional MART updates.

The $SNR_R$ is calculated by considering an average of regions inside and outside of the illuminated volume and is displayed in Fig. 10. The trend is similar to that observed earlier in the synthetic data (see Fig. 3): The $SNR_R$ of MART remains below 1.2 and MTE yields a value approximately 1.5. The $SNR_R$ of SMTE-MART increases along the sequence, requiring 15–30 frames to approach a value of 3. The SMTE results with a single MART iteration are poorer ($SNR_R < 2$) than those obtained with 3 or 5 iterations, confirming the previous observation and indicating that for experimental data, there is benefit in using more than a single MART update with SMTE-MART.

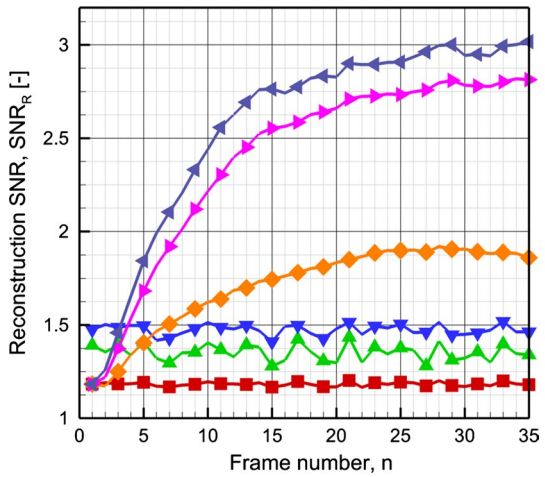


**Fig. 10** Reconstruction signal-to-noise ratio, $SNR_R$. Legend identical to Fig. 9

### 4.3 Velocity field analysis

A rendering of the instantaneous velocity field is shown in Fig. 11. The blue isosurfaces represent low-speed regions (50 % of the freestream velocity) throughout the velocity field. Brown isosurfaces indicate positive values of Q-criterion. A significant difference in the low-speed streaks is seen between MART and SMTE, the former being unable to capture the streaks throughout the entire streamwise direction. Furthermore, an improvement in the spatial coherence of the Q-criterion is evident in the SMTE result, which allows a less ambiguous identification of hairpin and cane structures.

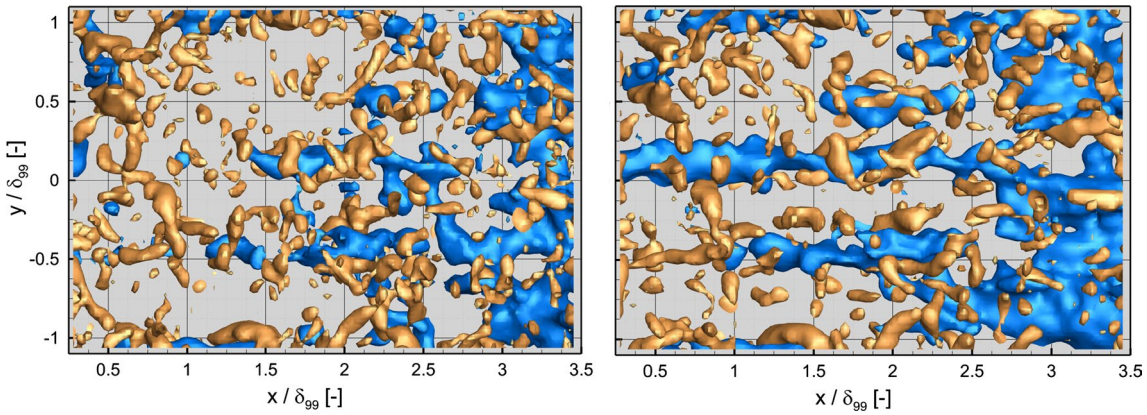


**Fig. 11** Instantaneous velocity field snapshot for frame $n = 30$ using MART (*left*) and SMTE $N_M = 5$ (*right*). *Blue isosurfaces* are streamwise velocity 50 % of the freestream velocity, and *brown isosurfaces* are of positive Q-criterion

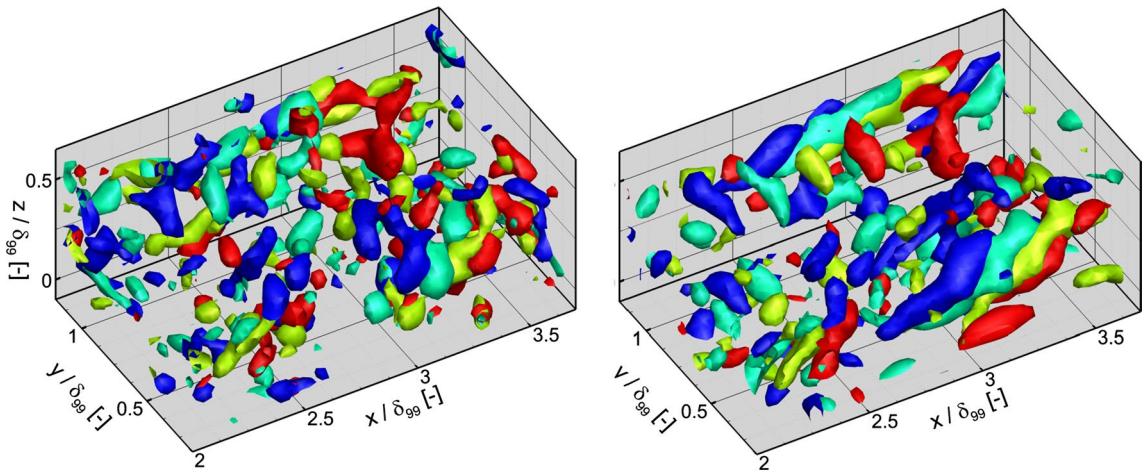


**Fig. 12** Overview of coherent structures identified by the Q-criterion for MART $N_M = 5$ (*left*) and SMTE $N_M = 5$ (*right*). Regions A and B designate two convecting hairpin structures

Time-resolved tomographic PIV has been recently used to investigate the temporal evolution of coherent structures (Schroder et al. 2011; Elsinga et al. 2012). The prediction of properties such as the lifetime of energy-containing eddies (Elsinga and Marusic 2010) and their stability strongly relies on an accurate description of their spatial pattern and their temporal evolution and the measurement noise plays a crucial role in biasing the estimate of such properties. The comparison of MART and SMTE is given here through visualization of these structures at subsequent recordings. In Fig. 12, a portion of the data is shown for four time instants where isosurfaces of Q-criterion are used to identify hairpin and cane structures. The isosurfaces are color-coded blue to red to designate subsequent time instants. A higher spatial and temporal coherence is observed for the results obtained with SMTE reconstruction. In contrast, the results based on the MART reconstruction are much more difficult to interpret in terms of time sequence.

A more objective assessment of the measurement precision is made invoking the assumption of incompressible flow whereby the velocity field divergence is zero. A nonzero measured value gives an estimate of the error in determining the tensor (Zhang et al. 1997) and further derived quantities such as the Q-criterion. A PDF of the divergence is given in Fig. 13 (left). Compared with MART, the SMTE exhibits a narrower distribution around zero, indicating a measurement better satisfying this condition. The performance of all methods throughout the sequence is associated to the standard deviation of the divergence and illustrated in Fig. 13 (right). Beginning from a nearly equal value at the start of the sequence, the SMTE decreases over approximately 10 frames to a value about 1.5 times less than MART (i.e., approximately 0.07 vox/vox from

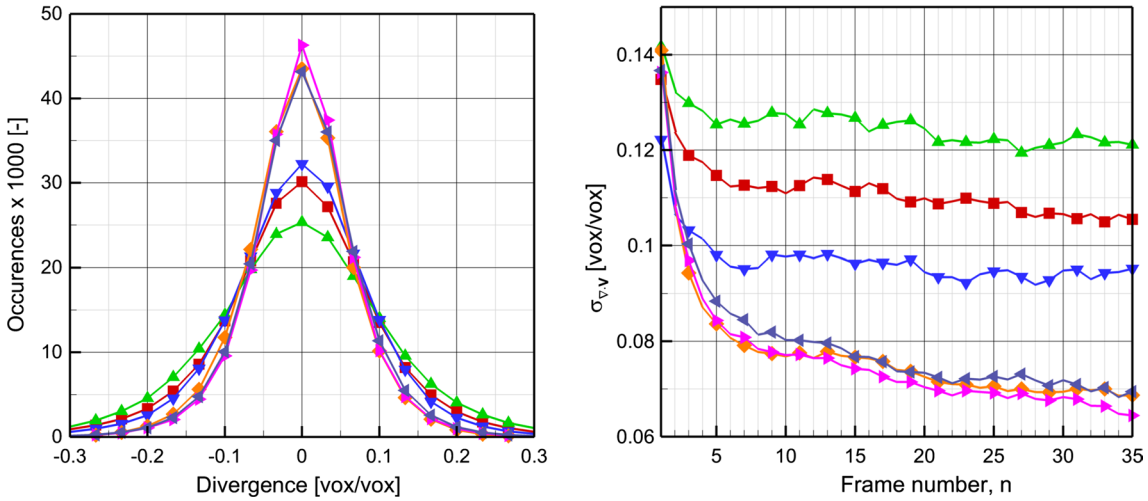


**Fig. 13** PDF of the divergence (*left*) for frame number $n = 30$, and standard deviation of the divergence (*right*) as a function of frame number. Legend identical to Fig. 9

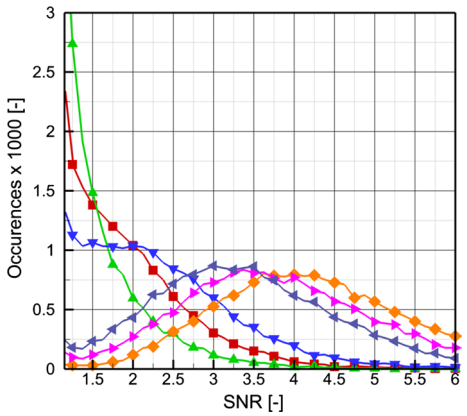


**Fig. 14** PDF of the correlation signal-to-noise ratio (SNR) for frame $n = 30$. Legend identical to Fig. 9

0.11 vox/vox). The decrease in divergence for the first 1–2 frames of normal MART cases is due to the time-marching predictor for the cross-correlation as mentioned earlier.

Finally, the robustness of the measurements is inquired using the cross-correlation signal-to-noise ratio (SNR), defined by the ratio of highest to second highest peak in the 3-D correlation map. A value >1.5 is often considered as acceptance criterion for a reliable correlation analysis (Keane and Adrian 1990). In Fig. 14, the PDF of SNR is shown for MART and SMTE. The former has a distribution with maximum occurrence in the range between 1.2 and 1.5. MTE is slightly shifted to higher values with a plateau up to a value of 2. The SMTE analysis is centered around a value of 3.5. The slight shift of the distributions with varying number of MART iterations in SMTE may not be regarded as an improvement in the measurement robustness. It is instead ascribed to the residual of the intensity field transported from the previous recording.

Assuming that velocity fluctuations are passively transported by the flow, the measurement precision can be estimated a posteriori making use of the space–time correlation function. The time that separates uncorrelated measurements is their temporal separation $\Delta t = 83$ μs. Novara and Scarano (2012) provided an estimate of the Lagrangian time scale for the intrinsic evolution of turbulent fluctuations, which was estimated in the order of 10 ms: two orders of magnitude longer than $\Delta t$. As a consequence, a high degree of correlation is expected between the velocity fields in a time series of 10–30 frames. Any rapid drop of the velocity spatiotemporal correlation peak from the unit value at the origin signals the presence of noisy fluctuations affecting the measurement.

The precision is therefore estimated by considering the drop of the maximum value of the spatiotemporal correlation function. A similar approach was followed by Sciacchitano et al. (2012) and Lynch and Scarano (2013). The spatiotemporal correlation function of the streamwise velocity component between two subsequent exposures separated by a time delay d$t$ and displacements d$x$, d$y$ and d$z$ is

$$\phi_u(\mathrm{d}x,\mathrm{d}y,\mathrm{d}z,\mathrm{d}t) = \frac{\sum_{i,j,k=0}^{N} u(i,j,k,t)\cdot u(i+\mathrm{d}x,j+\mathrm{d}y,k+\mathrm{d}z,t+\mathrm{d}t)}{\sqrt{\sum_{i,j,k=0}^{N} u(i,j,k,t)^2 \cdot \sum_{i,j,k=0}^{N} u(i+\mathrm{d}x,j+\mathrm{d}y,k+\mathrm{d}z,t+\mathrm{d}t)^2}} \quad (4)$$

where $N$ is the number of grid nodes in the measurement domain. The mean value of the velocity field is subtracted

prior to calculation, and the normalization guarantees that the result is bounded in the range between −1 and 1. The correlation of d$x$ with d$t$ (d$y$ and d$z$ set to zero) for the wall-normal velocity for MART, MTE-MART and SMTE are shown in Fig. 15. All results yield a similar advection velocity (indicated by the slope of the maximum $\phi$). However, the time over which the data are correlated is significantly shorter for the MART reconstruction (0.5 ms) in comparison with MTE (< 1 ms) and in particular SMTE (>1.5 ms).

To quantify the degree of correlation retained by SMTE, the three-dimensional spatiotemporal correlation is determined and the correlation peak is tracked in all three dimensions as a function of time. The peak value of the correlation function is shown in Fig. 16 for the streamwise (left) and wall-normal (right) velocity components. For the streamwise component, a reduction in correlation to 0.93 is noted for MART, compared with 0.94 for MTE and 0.96 for SMTE. This corresponds to relative error levels of 7, 6 and 4 % for the three methods, respectively. The wall-normal component is affected by larger errors, with a reduction to 0.86 for MART, 0.88 for MTE and 0.91 for SMTE.

## 5 Experimental assessment of a swirling jet

### 5.1 Test conditions and measurement apparatus

A second experimental test case demonstrates the utility of SMTE to treat experimental data obtained with fewer cameras, but at a seeding density typically practiced for systems with more cameras. The reduced cost and complexity of a tomographic PIV setup is attractive in realizing time-resolved tomographic PIV experiments.

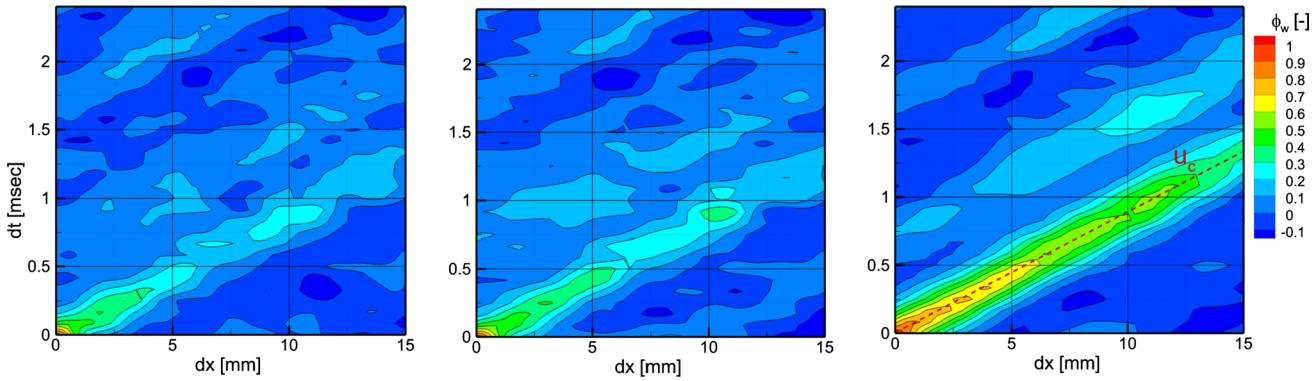


**Fig. 15** Spatiotemporal correlation of the wall-normal velocity as a function of time delay and streamwise shifts at a position 5 mm in height from the trailing edge. *Left* MART $N_M = 5$; *center* MTE-MART $N_M = 5$ $N_E = 2$ $N_O = 2$; *right* SMTE-MART $N_M = 5$, with an overlay of the estimated convection velocity $u_c$

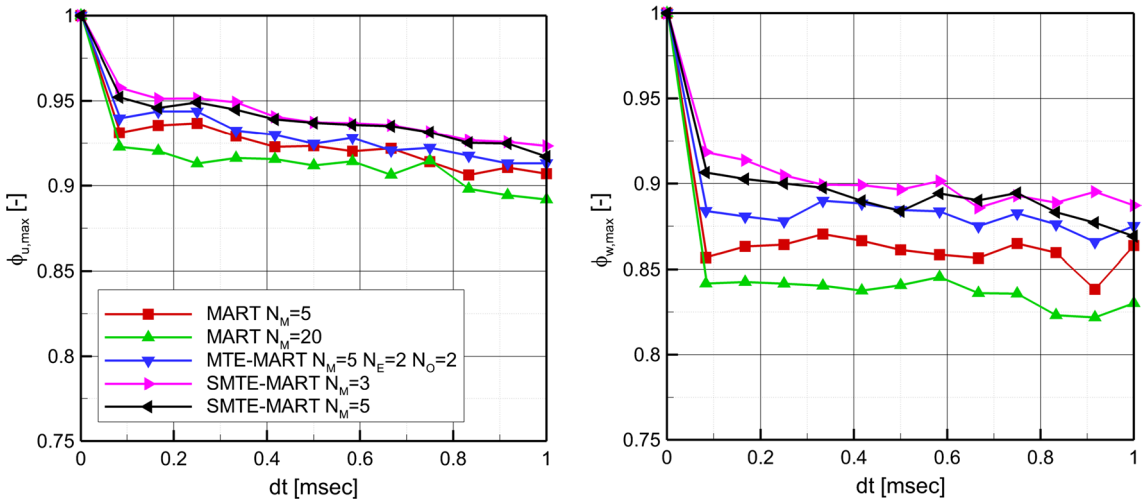


**Fig. 16** Maximum spatiotemporal correlation of the streamwise (*left*) and wall-normal (*right*) velocity as a function of time delay

Data are gathered from an experiment on low Reynolds number swirling jets conducted in the Jet Tomography Facility (JTF) at TUDelft. The jet consists of a 19.7-mm-diameter nozzle issuing vertically into a clear octagonal water tank (see Fig. 17). The swirl is introduced within the nozzle by a four-vane cylindrical channel insert. Immediately after the insert the nozzle ends sharply as a truncated pipe (Ianiro and Cardone 2012). The exit velocity is 0.05 m/s yielding a Reynolds number of 1000.

Neutrally buoyant polyamide particles with median diameter of 56 μm (VESTOSINT® 2157) are used as seeding particles. The water is recycled to maintain a constant seeding density equal to about 0.3 particles/mm$^3$. The illumination is provided by a Quantronix Darwin-Duo Nd/YLF laser (2 × 25 mJ/pulse @ 1000 Hz). The laser beam is shaped in order to feature a quasi-cylindrical illumination volume with a diameter approximately 50 mm at the top of the measurement domain and 45 mm at the nozzle exit.

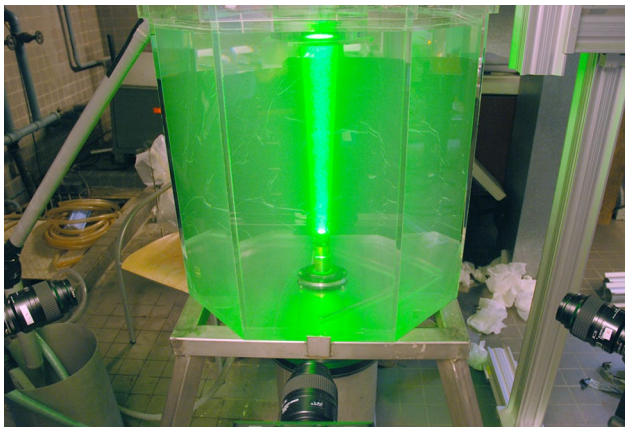

**Fig. 17** Photograph of swirling jet in the Jet Tomography Facility at TUDelft with three high-speed cameras viewing the measurement volume

Particle images are recorded by three LaVision Imager pro HS CMOS cameras (2016 × 2016 pixels, 11 μm pixel size) subtending an angle of 90°. Nikon objectives of 105 mm focal length are set with an aperture $f/\# = 22$ to provide focused imaging of the particles over the illuminated domain. This configuration yields a digital resolution of 18.6 pixels/mm. Images are acquired at 100 Hz, corresponding to maximum displacements of 10 voxels within the reconstructions. The particle image density is approximately ppp = 0.04 along the jet axis; for a three-camera system, this is a relatively high level of seeding density and the reconstruction quality factor Q is estimated below 0.8, as shown in Scarano (2013).

Image preprocessing consists only of dark image subtraction; no sliding minimum subtraction or smoothing is performed. The reconstructed volume is discretized by 850 × 2080 × 1000 voxels at 1.0 voxels/pixel. The cross-correlation analysis uses interrogation volumes of 48 × 48 × 48 voxels (2.6 × 2.6 × 2.6 mm$^3$) at 75 % overlap. This corresponds to $N_I = 6$ particles within an interrogation region.

### 5.2 Reconstruction quality

The reconstructed intensity field for MART and SMTE is shown in Fig. 18. Note that the illumination is cylindrical compared with the previous cases. The MART reconstruction shows a hexagonal pattern due to the formation of ghost particles in all regions where intersections of the camera lines of sight occur. The width of this hexagonal pattern is also not equal to the actual size of the illumination. After approximately 10 frames, SMTE retrieves a clear circular

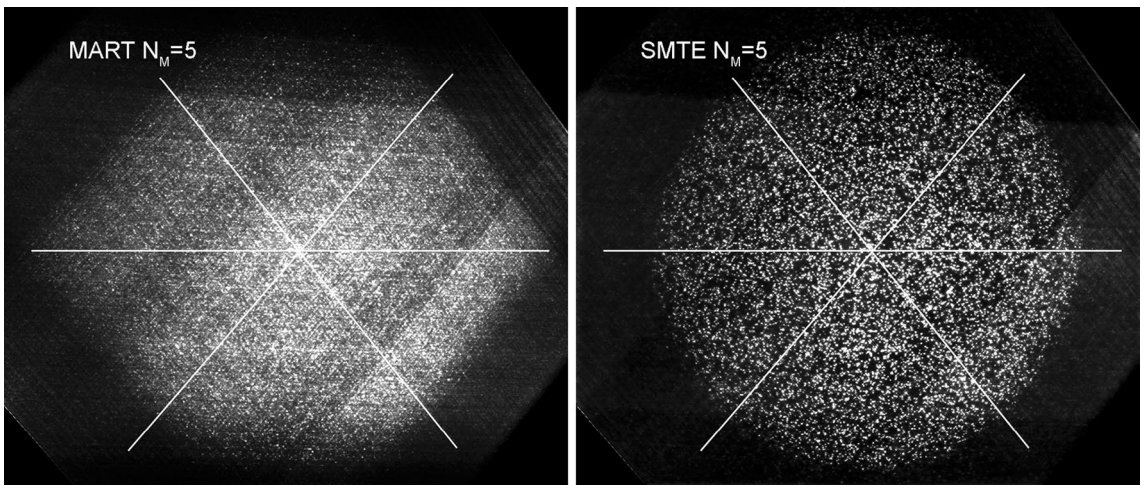


**Fig. 18** Reconstructed light intensity distribution. *White lines* indicate camera viewing directions

pattern for the intensity distribution. Moreover, individual particles are reconstructed with higher contrast and are clearly identified.

### 5.3 Velocity field analysis

A comparison of the velocity fields is shown in Fig. 19, aiming at confirming the more clear measurement of the flow structures. Gray isosurfaces denote the velocity magnitude equal to 70 % of the jet exit velocity. These isosurfaces trace the paths taken by the jets emanating from each of the four swirling vanes. A clear difference is noticed between MART and SMTE at the nozzle exit, where MART is unable to resolve one of the jet cores due to the contamination of the cross-correlation by slow-moving ghost particles generated by the surrounding quiescent fluid. The coherent vortical structures outlined by the blue isosurfaces also exhibit marked differences. The vortical pattern represented with the MART analysis has significant jitter, and a number of large-scale structures are strongly underestimated. The SMTE analysis recovers more information, improving the spatial and temporal coherence of structures throughout the velocity field.

## 6 Conclusions

The analysis of time-resolved tomographic PIV sequences can be performed in a computationally efficient and accurate manner on the basis of the MTE technique. A novel algorithm was introduced that replaces the *time-sliding-kernel* concept of the original MTE principle with the *time-marching* approach. For a given image sequence, the reconstruction of the previous frame is propagated in time using the velocity field and used as an enhanced initial guess for the following reconstruction. The method relies on time-resolved image sequences and is thus termed sequential MTE (SMTE).

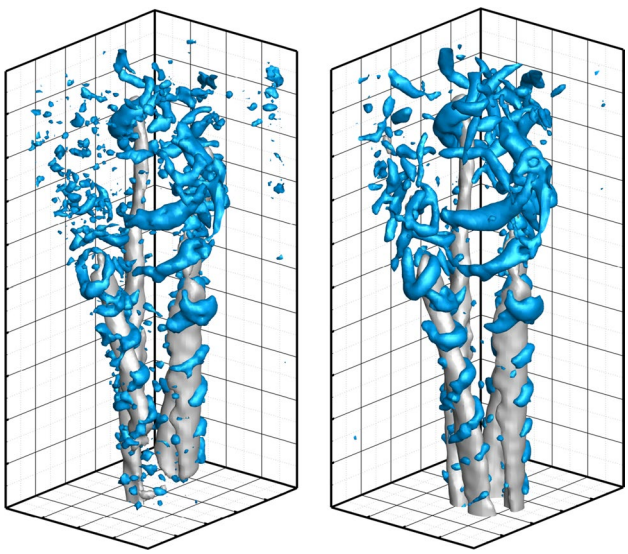

**Fig. 19** Velocity field comparison for the swirling jet at frame $n = 20$. *Left* MART $N_M = 5$; *right* SMTE $N_M = 5$. *Gray isosurfaces* at 70 % jet exit velocity, *blue isosurfaces* of positive Q-criterion

Synthetic tomographic PIV images generated from DNS of a turbulent boundary layer were used to evaluate the reconstruction and velocity error. After a sequence of 5–10 frames, SMTE was shown to significantly improve the reconstruction accuracy and to yield higher reconstruction signal-to-noise ratio, compared with standalone MART. The reduced presence of ghost particles reduced the random and bias errors of velocity field, particularly near the wall where the mean shear level is highest. Furthermore, the reduced number of reconstruction iterations needed by SMTE results in faster computations than MTE-MART and even of the standalone MART.

An experimental assessment on a densely seeded image sequence of an airfoil trailing edge showed an improvement in both reconstruction and velocity field quality compared with standalone MART. The SMTE technique retrieves the laser beam distribution within the reconstructed volume after approximately 20 frames, which was not possible for standalone MART and barely possible for MTE-MART. Although in the synthetic case a single MART update could be used for SMTE, it is observed that for experiments SMTE requires more than a single MART update to obtain accurate reconstructions across the sequence. Velocity fields obtained with SMTE reconstruction appear increased in their spatial and temporal coherence in comparison with standalone MART, confirmed by the evaluation of the divergence and the spatiotemporal velocity correlation function.

An experiment on a swirling jet showed that SMTE can also give important benefit for measurements using a three-camera system at seeding densities typically reserved for systems with more cameras. The combination of negligible computational cost of SMTE over standalone MART and the higher fidelity of the object reconstruction makes SMTE an attractive processing technique for time-resolved tomographic PIV datasets.

**Acknowledgments** The authors would like to thank Prof. Sergio Pirozzoli and Dr. Sergio Bernardini who performed the DNS simulation used in the present study, and Dr. Sina Ghaemi and Dr. Andrea Ianiro for the experimental datasets. Furthermore, the authors thank Dr. Matteo Novara for the useful discussion related to tomographic reconstruction. This research is supported by the European Community's Seventh Framework Programme (FP7/2007–2013) under the AFDAR project (Advanced Flow Diagnostics for Aeronautical Research). Grant agreement No. 265695.

## References

Adrian RJ (1997) Dynamic ranges of velocity and spatial resolution of particle image velocimetry. Meas Sci Technol 8:1393–1398

Adrian RJ (2007) Hairpin vortex organization in wall turbulence. Phys Fluids 19:041301

Atkinson C, Soria J (2009) An efficient simultaneous reconstruction technique for tomographic particle image velocimetry. Exp Fluids 47:553–568

Atkinson C, Buchmann N, Stanislas M, Soria J (2010) Adaptive MLOS-SMART improved accuracy tomographic PIV. In: 15th international symposium on application of laser techniques to fluid mechanics. Lisbon, Portugal

Bernardini M, Pirozzoli S (2011) Wall pressure fluctuations beneath supersonic turbulent boundary layers. Phys Fluids 23:085102

de Silva CM, Baidya R, Marusic I (2013) Enhancing Tomo-PIV reconstruction quality by reducing ghost particles. Meas Sci Technol 24:024010

Discetti S, Astarita T (2012) Fast 3D PIV with direct sparse cross-correlations. Exp Fluids 52:765–777

Discetti S, Natale A, Astarita T (2013) Spatial filtering improved tomographic PIV. Exp Fluids 54:1505

Elsinga GE, Marusic I (2010) Evolution and lifetimes of flow topology in a turbulent boundary layer. Phys Fluids 22:015102

Elsinga GE, Tokgoz S (2014) Ghost hunting–an assessment of ghost particle detection and removal methods for tomographic PIV. Meas Sci Technol 25:084004

Elsinga GE, Scarano F, Wieneke B, van Oudheusden BW (2006) Tomographic particle image velocimetry. Exp Fluids 41:933–947

Elsinga GE, Westerweel J, Scarano F, Novara M (2011) On the velocity of ghost particles and the bias errors in tomographic-PIV. Exp Fluids 50:825–838

Elsinga GE, Poelma C, Schroder A, Geisler R, Scarano F, Westerweel J (2012) Tracking of vortices in a turbulent boundary layer. J Fluid Mech 697:273–295

Ghaemi S, Scarano F (2010) Multi-pass light amplification for tomographic particle image velocimetry applications. Meas Sci Technol 21:127002

Ghaemi S, Scarano F (2011) Counter-hairpin vortices in the turbulent wake of a sharp trailing edge. J Fluid Mech 689:317–356

Huang HT, Fielder HF, Wang JJ (1993) Limitation and improvement of PIV, part II. Particle image distortion, a novel technique. Exp Fluids 15:263–273

Ianiro A, Cardone G (2012) Heat transfer rate and uniformity in multichannel swirling impinging jets. Appl Thermal Eng 49:89–98

Keane RD, Adrian RJ (1990) Optimization of particle image velocimeters: Part 1: Double pulsed systems. Meas Sci Technol 1:1202–1215

Lecordier B, Westerweel J (2004) The EUROPIV synthetic image generator (S.I.G.). In: Stanislas M, Westerweel J, Kompenhans J (eds) Particle image velocimetry: recent improvements. Springer, Berlin, pp 145–161

Lynch K, Scarano F (2013) A high-order time-accurate interrogation method for time-resolved PIV. Meas Sci Technol 24:035305

Lynch K, Scarano F (2014) Experimental determination of tomographic PIV accuracy by a 12-camera system. Meas Sci Technol 25:084003

Novara M, Scarano F (2012) Performances of motion tracking enhanced tomo-PIV on turbulent shear flows. Exp Fluids 52:1027–1041

Novara M, Batenburg KJ, Scarano F (2010) Motion tracking-enhanced MART for tomographic PIV. Meas Sci Technol 21:035401

Probsting S, Scarano F, Bernardini M, Pirozzoli S (2013) On the estimation of wall pressure coherence using time-resolved tomographic PIV. Exp Fluids 54:1567

Scarano F (2002) Iterative image deformation methods in PIV. Meas Sci Technol 13:R1–R19

Scarano F (2013) Tomographic PIV: principles and practice. Meas Sci Technol 24:012001

Scarano F, Moore P (2012) An advection-based model to increase the temporal resolution of PIV time series. Exp Fluids 52:919–933

Scarano F, Poelma C (2009) Three-dimensional vorticity patterns of cylinder wakes. Exp Fluids 47:69–83

Schanz D, Schroder A, Gesemann S, Wieneke B, Novara M (2013a) Non-uniform optical transfer functions in particle imaging: calibration and application to tomographic reconstruction. Meas Sci Technol 24:024009

Schanz D, Schroder A, Gesemann S, Michaelis D, Wieneke B (2013b) 'Shake The Box': a highly efficient and accurate Tomographic Particle Tracking Velocimetry (TOMO-PTV) method using prediction of particle positions. In: 10th International Symposium on Particle Image Velocimetry. Delft, Netherlands

Schanz D, Schroder A, Gesemann S (2014) 'Shake the box'–a 4D PTV algorithm: accurate and ghostless reconstruction of Lagrangian tracks in densely seeded flows. In: 17th international symposium on applications of laser techniques to fluid mechanics. Lisbon, Portugal

Schneiders JFG, Dwight RP, Scarano F (2014) Time-supersampling of 3D-PIV measurements with vortex-in-cell simulation. Exp Fluids 55:1692

Schroder A, Geisler R, Staack K, Elsinga GE, Scarano F, Wieneke B, Henning A, Poelma C, Westerweel J (2011) Eulerian and Lagrangian views of a turbulent boundary layer flow using time-resolved tomographic PIV. Exp Fluids 50:1071–1091

Sciacchitano A, Scarano F, Wieneke B (2012) Multi-frame pyramid correlation for time-resolved PIV. Exp Fluids 53:1087–1105

Thomas L, Tremblais B, David L (2014) Optimization of the volume reconstruction for classical Tomo-PIV algorithms (MART, BIMART, and SMART): synthetic and experimental studies. Meas Sci Technol 25:035303

Tsai RY (1987) A versatile camera calibration technique for high-accuracy 3D machine vision metrology using off-the-shelf TV cameras and lenses. IEEE J Robot Autom RA-3:323–344

van Oudheusden BW (2013) PIV-based pressure measurement. Meas Sci Technol 24:032001

Violato D, Scarano F (2013) Three-dimensional vortex analysis and aeroacoustic source characterization of jet core breakdown. Phys Fluids 25:015112

Westerweel J, Scarano F (2005) Universal outlier detection for PIV data. Exp Fluids 39:1096–1100

Wieneke B (2008) Volume self-calibration for 3D particle image velocimetry. Exp Fluids 45:549–556

Wieneke B (2013) Iterative reconstruction of volumetric particle distribution. Meas Sci Technol 24:024008

Zhang J, Tao B, Katz J (1997) Turbulent flow measurement in a square duct with hybrid holographic PIV. Exp Fluids 23:373–381